remote sensing

MDPI

Article

An Improved Descalloping Method Combined With Imaging Parameters for GaoFen-3 ScanSAR

Lihua Zhong [1,2,*], Xiaolan Qiu [1,2], Bing Han [1,2] and Yuxin Hu [1,2,3]

1 Institute of Electronics, Chinese Academy of Sciences, Beijing 100190, China; xlqiu@mail.ie.ac.cn (X.Q.); han_bing@mail.ie.ac.cn (B.H.); yxhu@mail.ie.ac.cn (Y.H.)
2 Key Laboratory of Technology in Geo-spatial Information Processing and Application Systems, Institute of Electronics, Chinese Academy of Sciences, Beijing 100190, China
3 School of Electronic, Electrical and Communication Engineering, University of Chinese Academy of Sciences, Beijing 100049, China
* Correspondence: lhzhong@mail.ie.ac.cn; Tel.: +86-010-5888-7208 (ext. 8949)

Received: 12 February 2020; Accepted: 1 March 2020; Published: 3 March 2020



Abstract: Due to the specific working mechanism of alternately transmitting and receiving signals between multiple adjacent swaths, scanning synthetic aperture radar (ScanSAR) will cause periodical wavelike modulation of the intensity image along azimuth direction, which is known as scalloping. Conventional descalloping methods are achieved by proper azimuth antenna pattern (AAP) correction and multi-looking techniques but are limited by the accuracy of Doppler centroid estimating and the thermal noise. Another type of method extracts and suppresses the scalloping texture on the image, but the scanning parameters of ScanSAR are insufficiently considered. The period of scalloping on the image is related to the period of switching between subswathes. While the harmonics can be calculated by the period of a periodic signal, an improved frequency filtering method combined with imaging parameters is proposed. The scalloping modulation model of ScanSAR combined with imaging parameters is constructed, and the harmonics of scalloping texture are accurately calculated and filtered. For the low signal to noise ratio (SNR) image, the antenna pattern is modified according to SNR to avoid scalloping caused by noise. For non-uniform scenes, scalloping suppression is achieved by using the scalloping features acquired by uniform scenes. To separate the non-uniform scenes from uniform scenes, we still use the characteristics of harmonics caused by scalloping. Our descalloping method achieves accurate suppression of scalloping without sea-land segmentation and ship mask and the residual scalloping is reduced from 1.0 to 0.3–0.5 dB. The residual scalloping and statistical characteristics of the image are analyzed to demonstrate the effectiveness of the proposed method.

Keywords: ScanSAR; scalloping; harmonics; imaging parameters; low SNR

1. Introduction

Scanning synthetic aperture radar (ScanSAR) periodically transmits and receives signals between adjacent subswathes to achieve wide range swath while sacrificing azimuth resolution [1]. Since SIR-C and RADARSAT-1 adopted ScanSAR mode, most spaceborne SAR systems are equipped with ScanSAR mode, such as ENVISAT, RADARSAT-2, TERRASAR-X, ALOS, etc. [2–6]. The latest launched RADARSAT Constellation Mission (RCM) still uses ScanSAR mode, not TOPS mode [7–9]. Due to the periodically switching between subswathes, scatters only sample part of the doppler history, and this will result in wavelike periodic modulation along the azimuth in the image, which is known as azimuth scalloping.

Scalloping is one of the important factors affecting the quality of the ScanSAR image, and another is the interscan banding (ISB) [10]. In this paper, we focus on the suppression of scalloping. In theory,

scalloping can be straightened out by precise compensation of azimuth antenna pattern (AAP) and multilooking techniques during the SAR imaging processing. The typical method is to compensate with the inverse AAP. Vigneron proved that with a higher signal to noise ratio (SNR), scalloping could be successfully removed [11]. Bamler proposed an algorithm that generates an optimum weighting function to suppress the scalloping and maximizes the equivalent number of looks (ENL) for a multilooking SAR system while the ENL is an important indicator of speckle noise [12–14]. Considering the Doppler centroid error and the shape error of AAP, Shimada designed a correction function that could better deal with the two errors, but could not obtain the maximum ENL [15]. In traditional methods, accurate Doppler centroid needs to be acquired for compensating the AAP accurately. However, due to the limitation of attitude measurement accuracy of spaceborne SAR satellite, Doppler centroid needs to be estimated from echo or image. As the doppler history is not continuous in ScanSAR, the traditional Doppler centroid estimation methods will be affected by the non-uniformity of the scene [16,17]. Some estimation methods for ScanSAR have been proposed [18,19]. Among them, Jin et al. proposed an estimation method that utilizes overlapping areas of adjacent burst images to avoid the impact of scene non-uniformity on the estimation results [20]. However, the estimation accuracy is affected by SNR. In low SNR areas such as the ocean, the estimation accuracy will be greatly degraded.

Although the descalloping techniques in the SAR processor have been developed, ScanSAR images with scalloping will still exist sometimes. Recently several post-processing descalloping techniques have been presented. These techniques treat scalloping as a periodic texture on the image and remove the texture from SAR images on the image or frequency domain. Typical methods include scalloping removal based on multi-scale analysis proposed by Schiavulli et al. [21]. Iqbal proposed a method to suppress scalloping using the Kalman filter on the ScanSAR image [22]. To retrieve wind field from the ScanSAR image with scalloping, Romeiser et al. proposed a frequency deconvolution method by utilizing the harmonics caused by the periodic scalloping in the frequency domain [23]. By ship mask and sea-land segmentation, the interference of the non-uniform scene to the sea spectrum is removed. By transforming the image of the pure sea surface to the frequency domain, the harmonics of scalloping are detected and separated from the spectrum of the sea. The descalloping methods of image domain also achieve good performance, but the ScanSAR imaging parameters are not given enough consideration while filtering the scalloping. Scalloping is closely related to ScanSAR's working mechanism and imaging parameters. Therefore, better scalloping suppression effect can be obtained by making full use of imaging parameters to optimize filtering processing.

Based on the work of Romeiser et al., this paper deduced the scalloping modulation model in the image domain combining with ScanSAR imaging parameters. According to the proposed model, a frequency domain filtering method is proposed. Moreover, the method considers the low SNR and non-uniform scene and provides solutions. Finally, we take ScanSAR images of China's GaoFen-3 (GF-3) satellite to analyze the descalloping performance and the statistical characteristics of the images before and after descalloping. Experimental results show that the proposed filtering method combined with imaging parameters can effectively suppress the scalloping in various scenes while keeping the backscatter coefficient and the statistical characteristics. The remainder of the paper is organized as follows. In Section 2, the ScanSAR working mechanism is described and the scalloping model for ScanSAR is analyzed. Several techniques of descalloping process including scalloping harmonics position calculation, noise modulation correction, and uniform scene selection are explained in Section 3. Experimental results based on the simulation and GF-3 real data are presented in Section 4, followed by some discussion of the experiments in Section 5. Section 6 draws the conclusions.

2. Scalloping Modeling for GF-3 ScanSAR Mode

GF-3 SAR has 12 operating modes, among which three are ScanSAR modes, namely narrow scanning (NSC), wide scanning (WSC), and global observation (GLO). The basic parameters of the three patterns are shown in Table 1 [24].

Table 1. Scanning synthetic aperture radar (ScanSAR) modes of GaoFen-3 (GF-3).

Observing Mode	Incidence Angle (°)	Nominal Resolution (m)	Nominal Swath (km)	Polarization
Narrow ScanSAR (NSC)	17–50	50	300	Dual
Wide ScanSAR(WSC)	17–50	100	500	Dual
Global observation (GLO)	17–53	500	650	Dual

ScanSAR modes of Gaofen-3 play an important role in the inversion of ocean parameters and ocean monitoring [25–27]. Take NSC as an example to illustrate the working mechanism of ScanSAR. The NSC employs three adjacent beams to compose the required 300km range swath, as shown in Figure 1.

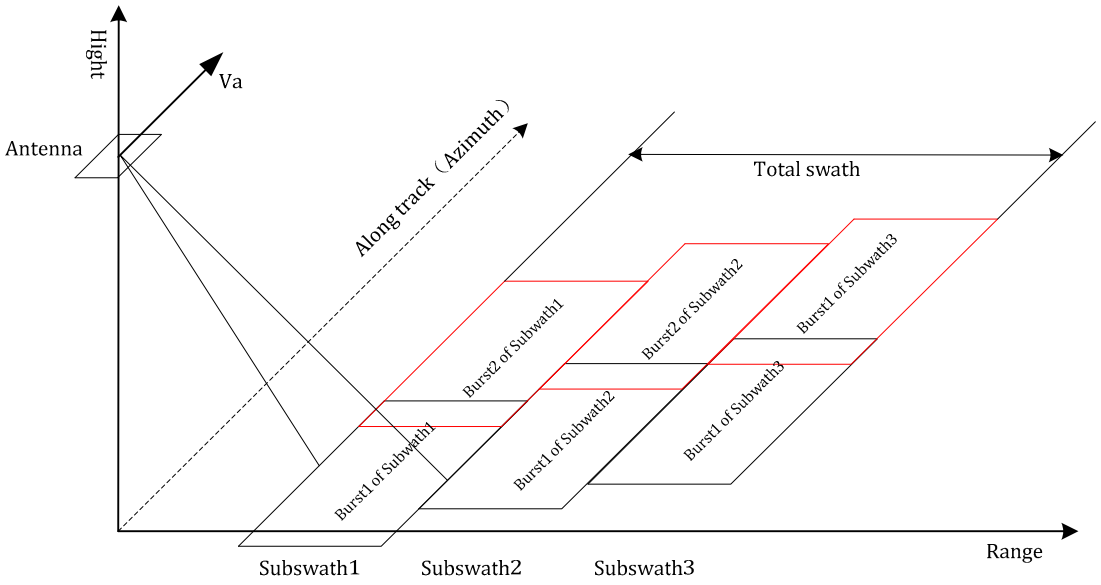


Figure 1. Narrow scanning (NSC) mode working diagram.

In NSC mode, the radar beam is switched periodically between subswath 1, subswath 2, and subswath 3. The corresponding dwell time of each subswath is T_1, T_2, and T_3 respectively. T_p is defined as cycle time of ScanSAR, and can be written as

$$T_p = \sum_{i=1}^{N} T_i \tag{1}$$

As the scalloping is caused by the discontinuous sampling in azimuth, one of the subswathes is selected to analyze the scalloping characteristics in the image domain.

It can be seen from Figure 2 that, due to the short dwell time of the radar beam in the subswath, each target is only irradiated by part of AAP, which leads to different doppler history and inconsistent intensity of target along the azimuth direction.

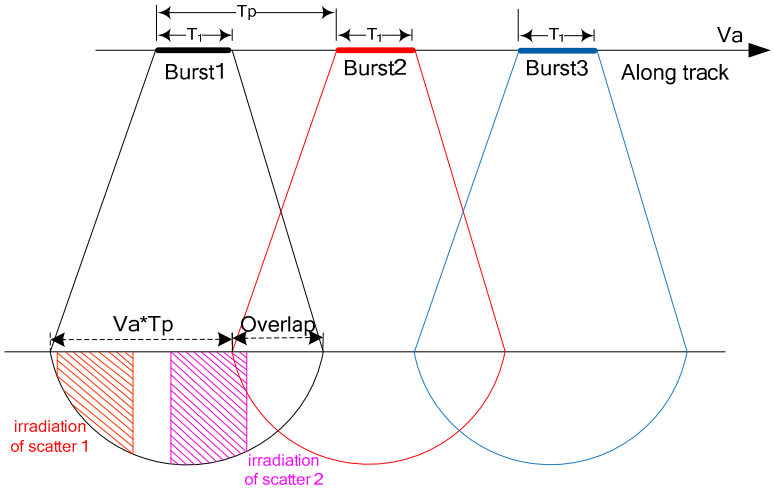


Figure 2. ScanSAR working sequence of a single subswath.

The model of i-th burst image after imaging processing is constructed in Equation (2) to analyze the scalloping in the image domain.

$$I_{bi}(x,r) = Ga(x)Gr(r)K(x,r)\sigma_{bi}(x,r) + K(x,r)W_{bi}(x,r) \tag{2}$$

where $I_{bi}(x,r)$ is the burst image. x and r represent the pixel position in $I_{bi}(x,r)$ in azimuth and range direction, respectively. $Ga(x)$ is the AAP, $Gr(r)$ is the range antenna pattern (RAP). $K(x,r)$ is the processing gain introduced by imaging processing. $\sigma_{bi}(x,r)$ is the backscattering coefficient of burst i. $W_{bi}(x,r)$ is the thermal noise of the SAR system during burst i. Here we consider the azimuth scalloping phenomenon for each range gate, so we ignore $K(x,r)$ and $Gr(r)$ because they are approximately constant along the azimuth direction. The image model of burst i along azimuth can be written as

$$I_{bi}(x) = Ga(x)\sigma_{bi}(x) + W_{bi}(x) \tag{3}$$

The subswath image $I(x)$ is obtained by stitching each burst image $I_{bi}(x)$ along the azimuth direction. Usually, the thermal noise $W_{bi}(x)$ can be considered as invariant for each burst. Therefore, we have the following equation:

$$\begin{aligned} I(x) &= \textstyle\sum_{i=1}^{N} I_{bi}(x - i * Np) \\ &= Gx(x)\sigma(x) + W(x) \end{aligned} \tag{4}$$

where Np is the period on image domain respect to T_p. N is the number of bursts along azimuth. $\sigma(x)$ and $W(x)$ are the backscattering coefficient and noise of the whole image, respectively, and are obtained by summing $\sigma_{bi}(x)$ and $W_{bi}(x)$ along azimuth. When AAP of each burst is consistent, $Gx(x)$ is a periodic function, as shown in Equation (5).

$$Gx(x) = \sum_{i=1}^{N} Ga(x - i * Np) \tag{5}$$

We use $1/Gx(x)$ to apply azimuth radiometric correction. The corrected image can be expressed as Equation (6).

$$I'(x) = \frac{I(x)}{Gx(x)} = \sigma(x) + W(x)/Gx(x) \tag{6}$$

However, the Doppler Centroid error will lead to an azimuth shift Δx in $1/Gx(x)$. Therefore, the actual correction function is $1/Gx(x+\Delta x)$ instead of $1/Gx(x)$. Equation (6) can be written as follows.

$$I'(x) = \frac{I(x)}{Gx(x+\Delta x)} = \frac{Gx(x)\sigma(x)}{Gx(x+\Delta x)} + \frac{W(x)}{Gx(x+\Delta x)} \tag{7}$$

The mismatch between $1/Gx(x)$ and $1/Gx(x+\Delta x)$ causes the scalloping, as shown in Figure 3.

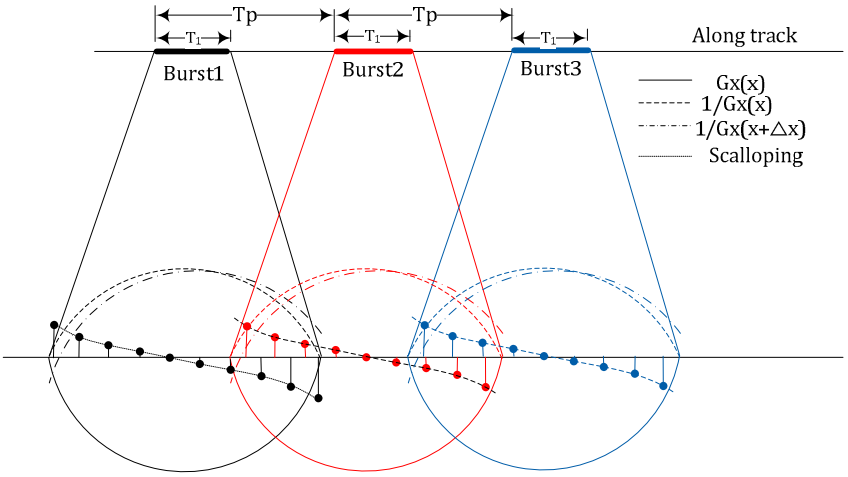


Figure 3. ScanSAR azimuth antenna pattern correction and scalloping schematic diagram.

The period of the scalloping in the image domain, Np, is therefore related to the period of the burst pattern through the azimuth velocity V_a and the pixel space along azimuth da, as shown in Equation (8).

$$Np = T_P * V_a / da \tag{8}$$

The image model modulated by scalloping can be derived from Equations (7) and (8).

$$I'(x) = \sigma(x) \sum_{i=1}^{N} Sca(x - i * Np) + W'(x) \tag{9}$$

where $Sca(x)$ represents the scalloping modulation caused by the mismatch between $1/Gx(x)$ and $1/Gx(x+\Delta x)$. $W'(x) = \frac{W(x)}{Gx(x+\Delta x)}$ is the thermal noise modulated by $1/Gx(x+\Delta x)$.

The mismatch of $1/Gx(x)$ and $1/Gx(x+\Delta x)$ during AAP correction causes the so-called scalloping, which is the first term in Equation (9). However, when the image's SNR is relatively low, the noise modulated by AAP also exhibits a periodic texture, which may also be referred to as scalloping (the second term in Equation (9)). The above two reasons that caused scalloping will be analyzed separately.

The AAP is usually compensated in the Doppler frequency domain. In the ECS imaging algorithm used by GF-3 [28–30], the residual scalloping has a linear correspondence with the Doppler centroid error. Taking GF-3 as an example, we analyze the variation of the residual scalloping with the Doppler centroid error.

Figure 4a shows the AAP of ScanSAR mode. The antenna length of GF-3 is 15 m (azimuth) × 1.232 m (elevation) in size and the azimuth beamwidth is about 0.2° [24]. Figure 4b shows the relationship between scalloping and Doppler centroid error. Scalloping varies approximately linearly with Doppler centroid error. According to the attitude measurement accuracy and AAP of the GF-3 satellite [31,32], the Doppler centroid calculation error can reach 100 Hz. It can be seen from Figure 4b that the maximum scalloping introduced by the Doppler Centroid error is about 3.5dB. Although it can be improved by Doppler centroid estimation, the residual scalloping can still reach 1.0–1.5 dB, especially under low SNR scenes such as sea surface.

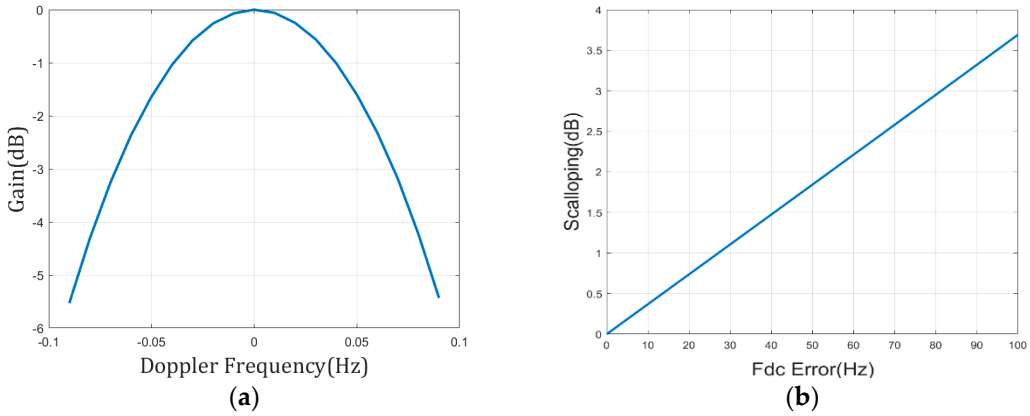


Figure 4. Relationship between azimuth antenna pattern (AAP), Doppler centroid error, and scalloping: (**a**) main lobe of AAP; (**b**) relationship between Doppler centroid error and scalloping.

Noise is another important factor that strengthens the scalloping. During the process of AAP correction, the noise is modulated by AAP. Due to the different Doppler history of each point along azimuth direction in the ScanSAR image, the irradiation power of pixels along azimuth direction is also different, resulting in worse SNR at the edge of AAP, which is also the edge of the burst image. Figure 5 shows the contribution of noise to scalloping in a single burst image with different SNR under the assumption of uniform scene. In Figure 5, we ignore the Doppler Centroid error and the shape error of AAP and only consider the influence of thermal noise.

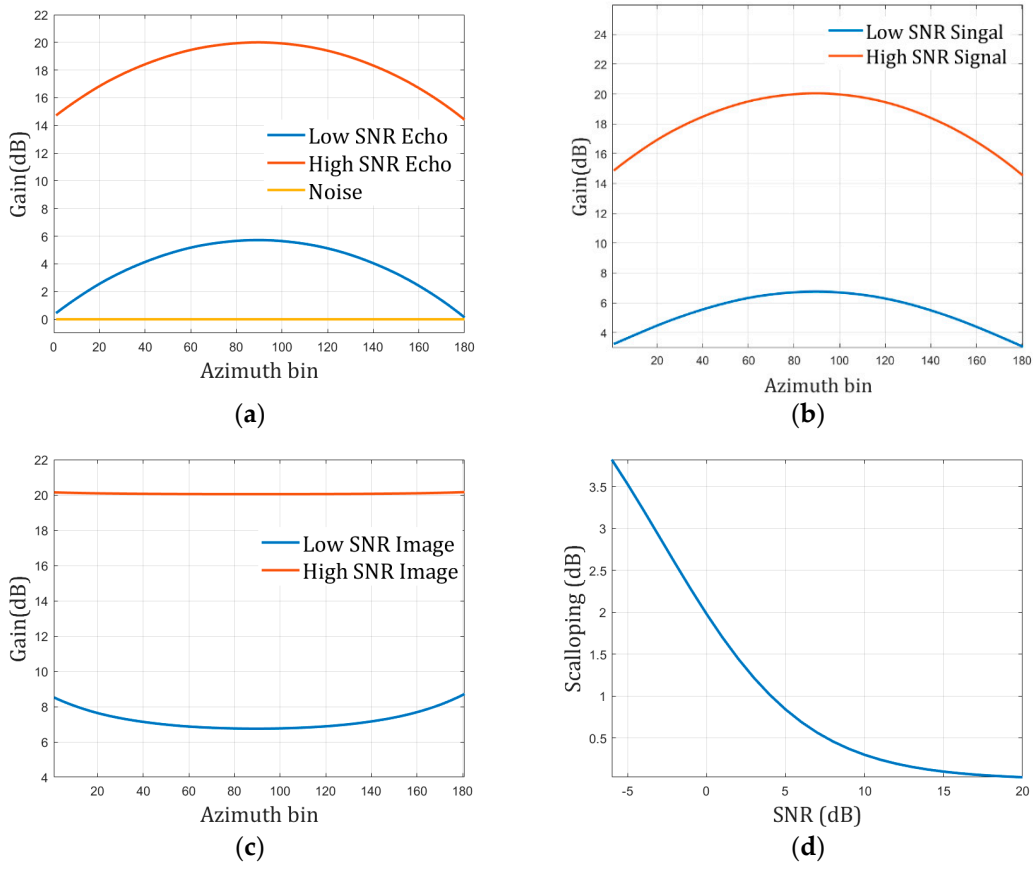


Figure 5. Image radiometric correction schematic diagram of ScanSAR with different signal to noise ratios (SNRs): (**a**) echo of different SNR and noise; (**b**) added noise to echo of different SNR; (**c**) after AAP correction of (**b**); (**d**) relationship between scalloping and SNR.

For the scene with SNR of 0 dB at the edge of AAP, the scalloping introduced by noise can reach 1.98dB. Normally, the Noise Equivalent Sigma Zero ($NE\sigma_0$) of the SAR system is about -21dB [24] while σ_0 of sea surface is also about -20dB at high incident in C-band [33]. Therefore, for the scenario of low SNR, such as the ocean, noise becomes the main factor that causes scalloping.

3. Improved Descalloping Method Based on Imaging Parameters

3.1. Scalloping Harmonics Position Calculation

When SNR of the image is high enough (for example higher than 10dB while scalloping caused by noise lower than 0.3dB in Figure 5d), the influence of noise in Equation (9) can be ignored, and the periodic modulation image model is simplified as Equation (10)

$$I'(x) = \sigma(x) \sum_{i=1}^{N} Sca(x - i * Np) \tag{10}$$

Transforming the image $I'(x)$ to logarithmic image $I_{log}(x)$, the relationship between the two terms on the right hand of Equation (10) changes from multiplication to addition.

$$I_{log}(x) = 10 * \log_{10} \sigma(x) + 10 * \log_{10} \sum_{i=1}^{N} Sca(x - i * Np) \tag{11}$$

Changing $I_{log}(x)$ from image domain to frequency domain $F(k)$, the azimuth spectrum of $I_{log}(x)$ consists of the spectrum of the scene and spectrum of the residual scalloping, as shown in Equation (12).

$$F(k) = F_{\sigma}(k) + F_{sca}(k) \tag{12}$$

where $F_{\sigma}(k)$ and $F_{sca}(k)$ are the Fourier transform of $10 * \log_{10} \sigma(x)$ and $10 * \log_{10} \sum_{i=1}^{N} Sca(x - i * Np)$, respectively.

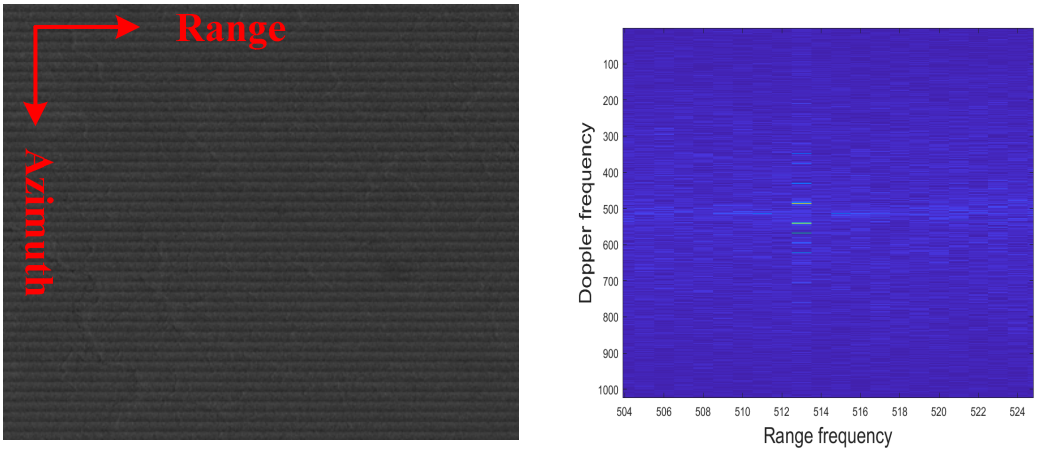
The residual scalloping is a periodic signal along the azimuth in the image domain. The spectrum of the periodic signal can be expressed as a set of equal-spaced harmonics. The location of the harmonic is related to the period of the signal. In our case, it can be calculated by Equation (13).

$$k_i = \frac{i * N_{fft}}{Np} \quad -Np/2 \le i \le Np/2 \tag{13}$$

k_i is the position of ith harmonic in frequency domain, and N_{fft} is the number of points of fast Fourier transform (FFT) when transforming to frequency domain.

We took the Amazon rainforest image of GF-3 as an example to show the spectral characteristics of harmonics caused by scalloping. Due to the uniformity within an area of hundreds of kilometers, the Amazon rainforest is often used in SAR radiometric quality analysis.

As can be seen from Figure 6a, in the GF-3 ScanSAR image, the scalloping is parallel to the range direction. In the power spectrum of the image, as shown in Figure 6b, the harmonics caused by the scalloping are perpendicular to the range direction and are all distributed near the center of the range spectrum (0 frequency). The power spectrum distribution at the center of the spectrum is shown in Figure 7.



(**a**) (**b**)

Figure 6. Amazon rainforest image of GF-3: (**a**) part of the Amazon rainforest image of GF-3 NSC mode; (**b**) power spectrum of (**a**).

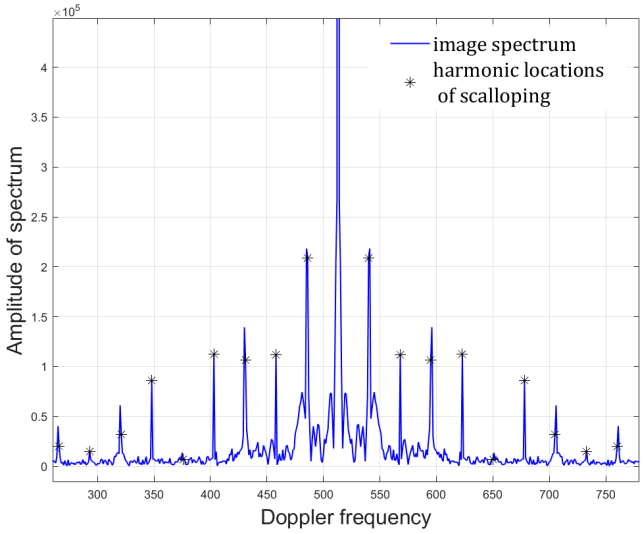


Figure 7. The harmonics caused by scalloping in uniform scene.

In Figure 7, the calculated positions of harmonics exactly match the spectrum of the image. We can see that some calculated harmonics are not located at the peak of the spectrum, because k_i in Equation (13) is generally not an integer and we plot the harmonics at the nearest integer of k_i.

3.2. Noise Modulation Correction

Parameter inversion usually uses the σ_0 of the scene. Taking GF-3 as an example, according to GF-3 user manual, the method of obtaining σ_0 in GF-3 image is as follows.

$$\sigma^0_{dB}(x,r) = 10 * \log_{10} I(x,r) - K_{dB} \tag{14}$$

where K_{dB} is the calibration constant value obtained by calibration through the reflector. In order to eliminate the influence of noise, it is usually necessary to subtract noise power from the image. The specific methods are as follows

$$\sigma^0_{dB}(x,r) = 10 * \log_{10}(I(x,r) - P_N(r)) - K_{dB} \tag{15}$$

Noise power $P_N(r)$ is generally a set of values that varies along the range direction according to the modulation of RAP and the imaging processing gain. However, the modulation of AAP in ScanSAR mode is not considered in the given noise power, which is constant for different pixels in the StripSAR image but varies along azimuth in the ScanSAR image. Considering the special working mechanism of ScanSAR, it is difficult to give out the power of noise variation in both range and azimuth direction.

After the AAP is corrected in Equation (6), $\sigma(x)$ can be obtained by ignoring the modulated noise $\frac{W(x)}{Gx(x)}$, and the image intensity reflects σ_0 of the target. Considering the effect of noise, if we still want to get σ_0 from the image, a modified AAP $Gx'(x)$ should be used to replace $Gx(x)$, as shown in Equation (16).

$$I'(x) = \frac{Gx(x)\sigma(x)}{Gx'(x)} + \frac{W(x)}{Gx'(x)} = \sigma(x) \tag{16}$$

where $Gx'(x)$ is the new AAP that we wanted. The power of $W(x)$ can be obtained through the system thermal noise obtained by noise calibration and imaging processing gain. The SNR of the image can be expressed as Equation (17).

$$SNR(x) = \frac{Gx(x)\sigma(x)}{W(x)} = \frac{I(x) - W(x)}{W(x)} \tag{17}$$

Submitting Equation (17) into Equation (16), modified AAP can be expressed as Equation (18).

$$Gx'(x) = Gx(x)\left(1 + \frac{1}{SNR(x)}\right) \tag{18}$$

$Gx'(x)$ is used to replace $Gx(x)$ for the correction of AAP. This derivation is consistent with Freeman's analysis of the influence of noise [34]. The scalloping caused by noise is weakened and the residual scalloping is mainly caused by the Doppler Centroid error.

3.3. Uniformity Scene Selection

In the method of Romaier et al., it is necessary to perform sea–land segmentation and ship mask for the image to be processed, because the non-uniform scene causes the harmonics of the scalloping to be submerged in the scene spectrum, and the harmonics of the scalloping cannot be extracted. Figure 8 shows a typical ScanSAR image with a non-uniform scene, which will be used to analyze the characteristics of scalloping in the non-uniform scene.

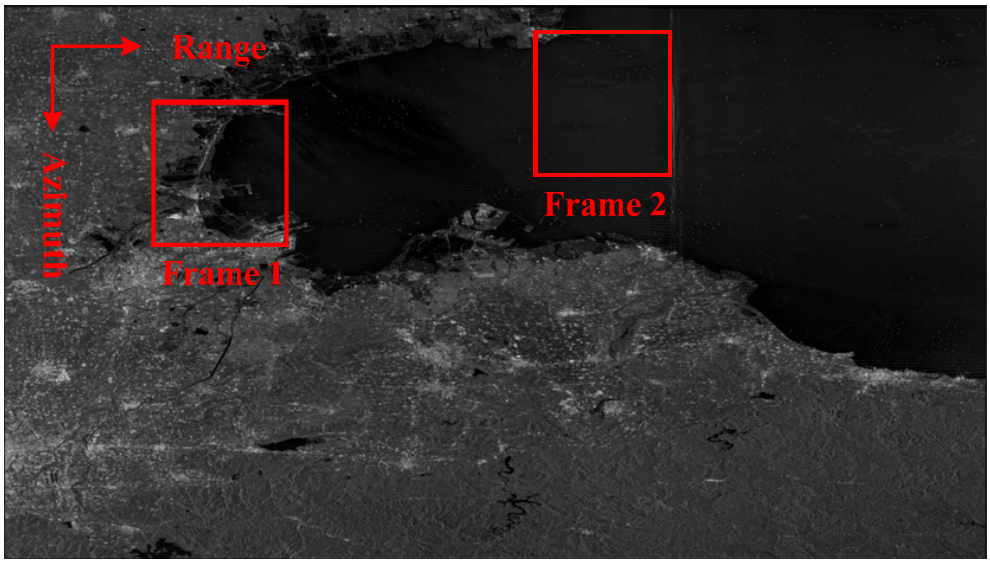


Figure 8. Non-uniform image obtained by GF-3: Scene ID:4295848; Imaging Mode: NSC; Polar Mode: HH; Date: 2017-11-05; Area: Bohai bay, China.

Figure 8 is the ScanSAR image of Bohai bay acquired by GF-3 on November 5, 2017. There are densely distributed vessels in Bohai Bay, and many port infrastructures and maricultural facilities on the shore. Two regions marked by red frames in Figure 8 were selected to show the frequency spectrum in Figure 9. Frame 1 in Figure 8 contains port facilities and Frame 2 contains lots of vessels.

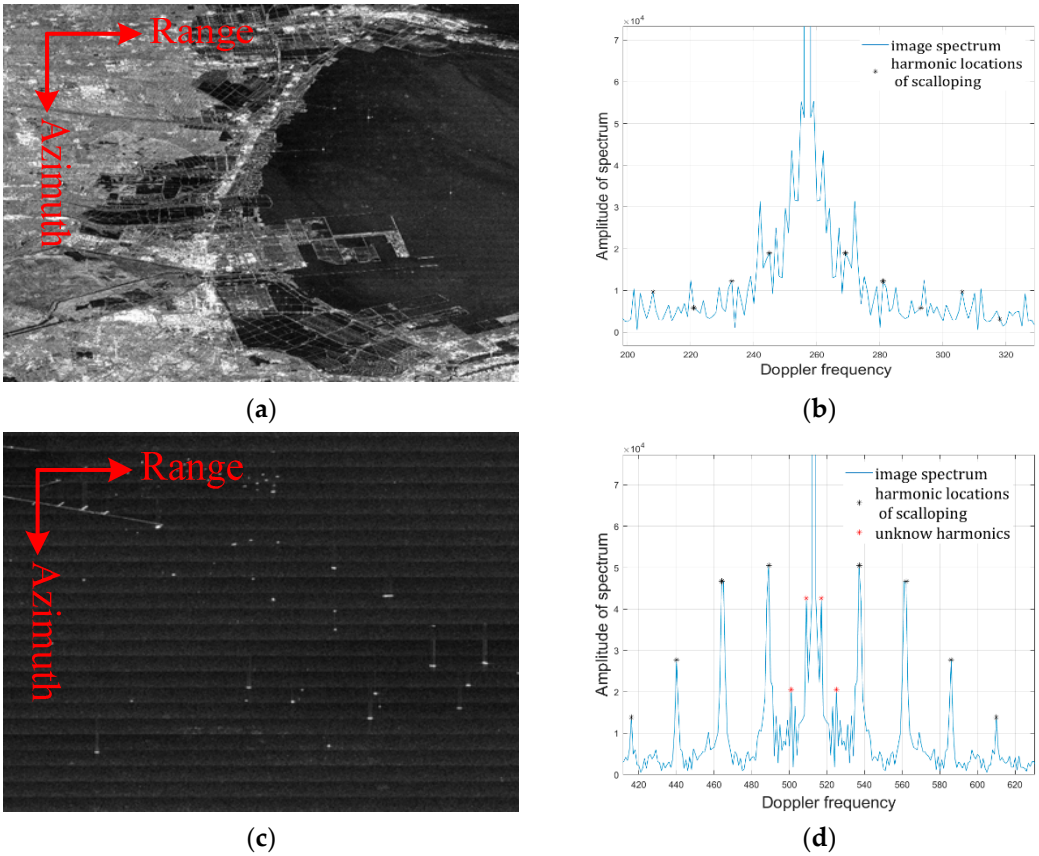


Figure 9. Spectrum characteristics of scalloping in non-uniform scene: (**a**) the region near Bohai bay of Frame 1 in Figure 8; (**b**) the scalloping spectrum of (a); (**c**) the region with densely distributed vessels of Frame 2 in Figure 8; (**d**) scalloping spectrum of (c).

As can be seen from Figure 9a, artificial buildings in the image, such as fences for seaside aquaculture, are also approximately periodic which would lead to harmonics and may be regarded as harmonics of scalloping in the frequency domain. In Figure 9b, the harmonics of scalloping are submerged under the spectrum of the scene, and multiple strong peaks appear in the spectrum of the scene. In Figure 9d, the harmonics of scalloping are not submerged, but two groups of new harmonics introduced by dense ships have appeared. However, the locations of the harmonics introduced by ships are different from that of scalloping.

We see that for uniform scenes, such as the Amazon rainforest in Figure 7, the harmonics of scalloping protrude above the surrounding spectrum. In non-uniform scenes, as shown in Figure 9b, the harmonics of scalloping are submerged by the surrounding spectrum. Therefore, we can use this feature to distinguish between uniform and non-uniform scenes. We calculated the ratio of the signal intensity at the harmonic frequency of the scalloping to the average signal strength of the surrounding spectrum (usually averaging the spectral intensity of the surrounding 8–10 points and avoiding two points near the scalloping harmonic). When the intensity of the largest two sets of harmonics was stronger than the surrounding spectrum by 10 dB, we determined that the scene was uniform.

At the same time, we also found that although periodically densely distributed ships introduce new harmonics into the spectrum, the position of the harmonics is different because the period of the ship's distribution is different from the period of scalloping. Since we can accurately calculate the

positions of scalloping harmonics, the harmonics introduced by the ships do not affect the extraction and suppression of the scalloping harmonics. Therefore, the sea surface containing ships was also considered to be a uniform scene in this paper.

3.4. Processing Flowchart

The flow chart of the proposed descalloping method in this paper is shown in Figure 10.

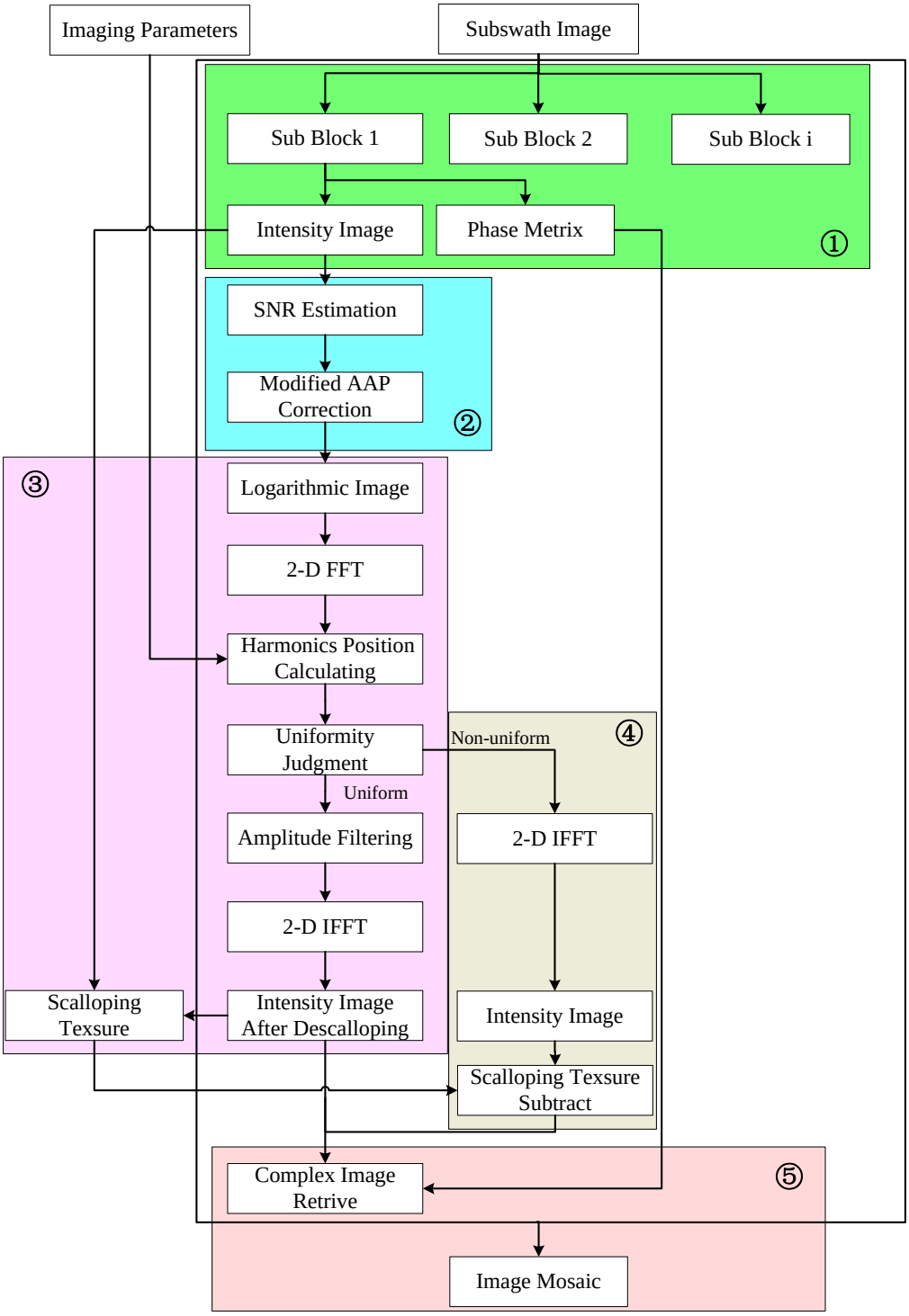


Figure 10. Flow chart of the improved descalloping method combined with imaging parameters.

As can be seen from Figure 10, the algorithm proposed in this paper can be divided into five steps.

Step 1: The subswath image of ScanSAR is separated into subblock images with a certain size for processing in parallel, which can not only improve the processing efficiency but also ensure that the scene changes slowly within each subblock image. According to the research and test, for the ScanSAR image of GF-3 satellite, block sizes of 256 pixels in range and 1024 pixels in azimuth are adopted, which can not only meet the requirements of FFT but also obtain better descalloping effect. The method of overlapping partition is adopted to improve the processing effect on block edges. The range and azimuth overlapping pixels are 32 and 64, respectively. When the input image is complex, to maintain phase information, for each block image, the amplitude and phase are extracted, respectively, and stored as intensity matrix $I(x, r)$ and phase matrix $\varphi(x, r)$.

Step 2: The SNR can be estimated by the inner-calibration data or from the range spectrum of the raw data [34]. For the high SRN image, the traditional AAP correction method is adopted, for low SNR image, using corrected AAP to replace traditional AAP for correction.

Step 3: After converting the intensity image $I(x, r)$ into logarithmic representation according to Equation (9), we change the logarithmic image into the frequency domain by two-dimension FFT and calculate the position of the harmonic k_i by Equation (13). Separating uniform scenes from non-uniform scenes by the ratio between the intensity of harmonics and mean intensity surrounds the harmonics. For uniform scenes, the amplitude of the harmonics is filtered by median filtering while the phase preserves the original value. Since k_i is generally not an integer, it is necessary to filter the frequency points of $\lfloor k_i \rfloor$ and $\lceil k_i \rceil$. $\lfloor k_i \rfloor$ and $\lceil k_i \rceil$ are integers round down and round up of k_i. The spectrum after filtering is transformed by inverse FFT(IFFT), and then the subblock image after scalloping suppression is obtained by transforming the exponential image to the intensity image. Subtracting the original subblock image with the descalloped image to obtain the scalloping texture.

Step 4: For non-uniform scene, changing the data back to the image domain by two-dimension IFFT. Subtracting the original subblock image with the scalloping texture obtained in Step 3 to suppress scalloping in non-uniform scenes.

Step 5: The intensity subblock images are splicing into the original subswath images, and the complex subswath images are reconstructed by adding the phase information $\varphi(x, r)$.

4. Experimental Results

4.1. Simulation Experiment

4.1.1. ScanSAR Image Simulation

The radiometric characteristics and statistical characteristics of SAR image are key factors for applications such as ship detection, classification, and identification, parameter inversion, and so on. Therefore, we analyzed and verified the radiometric accuracy and statistical characteristics of the image before and after the scalloping suppression. The difficulty in analyzing radiometric and statistical properties means that we could not obtain the true value of radiometric and statistical properties of the ScanSAR image, so that the improvement of scalloping suppression cannot be quantitatively evaluated. In the GF-3 satellite, the antenna beams of ScanSAR mode are the same as standard strip (SS) mode [24]. In order to obtain the true value for comparison, we used the GF-3 SS image to simulate the ScanSAR image, and took the characteristics of the SS image as the true value.

We used the GF-3 SS mode image to simulate the NSC mode image according to the characteristic parameters of the scalloping in the NSC mode. The SS mode image was acquired by GF-3 on 29 June 2018, as shown in Figure 11a. The pixel spacing of the SS image is 5.74 × 4.50 m in azimuth and range, respectively, and the image pixel spacing of the NSC mode is 20 × 13.5m, so the SS image is downsampled three times along the azimuth direction and three times along the range direction. On the downsampled image, a periodic linear modulation with a period of 42 pixels and an amplitude of 1.6 dB was multiplied along the azimuth, as shown in Figure 11b. The simulated scalloping image is shown in Figure 11c.

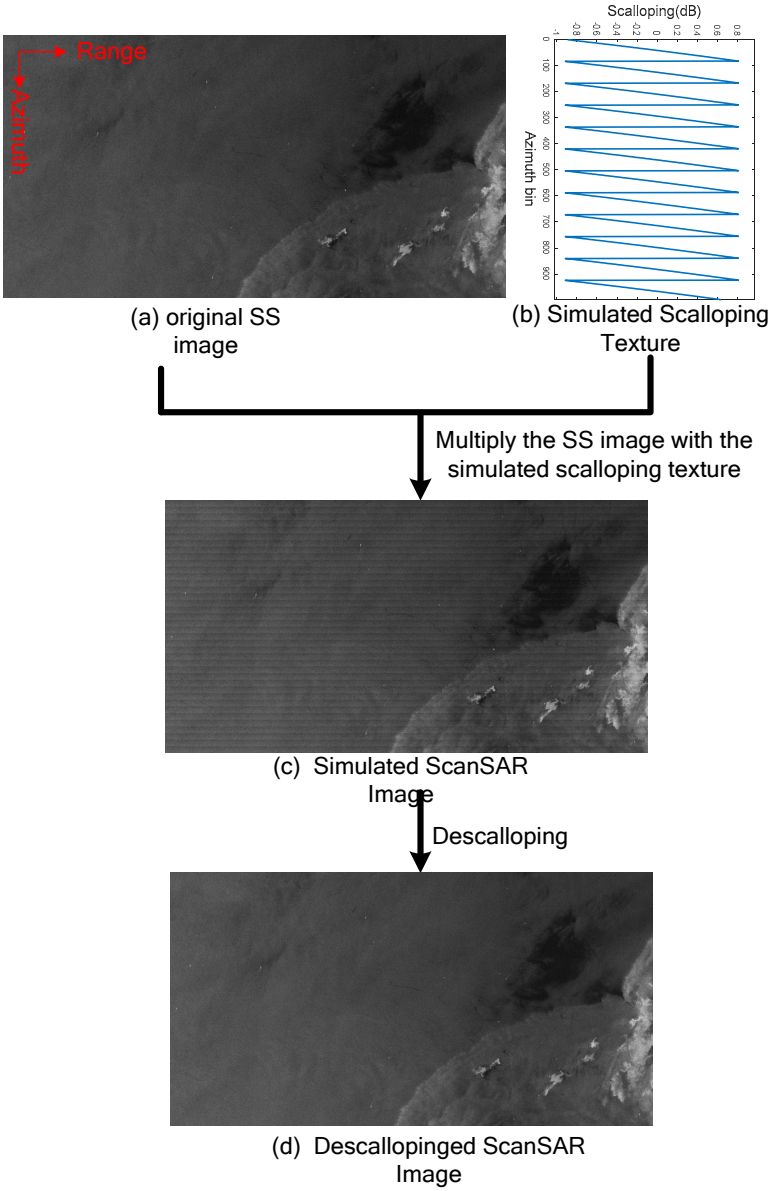


Figure 11. ScanSAR image simulation schematic diagram.

In the following sections, we will analyze and discuss the radiometric and statistical characteristics of Figure 11c,d, and compare the results with Figure 11a.

4.1.2. Radiometric Characteristics Analysis

The depth of scalloping was measured using the technique described in [35]. The data were integrated along the range direction to estimate the average power in each azimuth line. The depth of the scalloping is given as the ratio of maximum to minimum local powers. A summation of pixel powers, DN_{ij}^2, is completed along the scalloping contours $j(i)$.

$$P(i) = \sum_{j(i)} DN_{ij}^2$$

$$\Delta P = 10 * \log_{10}\left\{\frac{max[P(i)]}{min[P(i)]}\right\} \quad (19)$$

The scalloping causes the image to have uneven radiometric characteristics along the azimuth. We analyzed the scalloping suppression effect according to Equation (18). The scalloping suppression effects of the stationary sea surface and the non-stationary sea surface were analyzed and the results are shown in Figure 12.

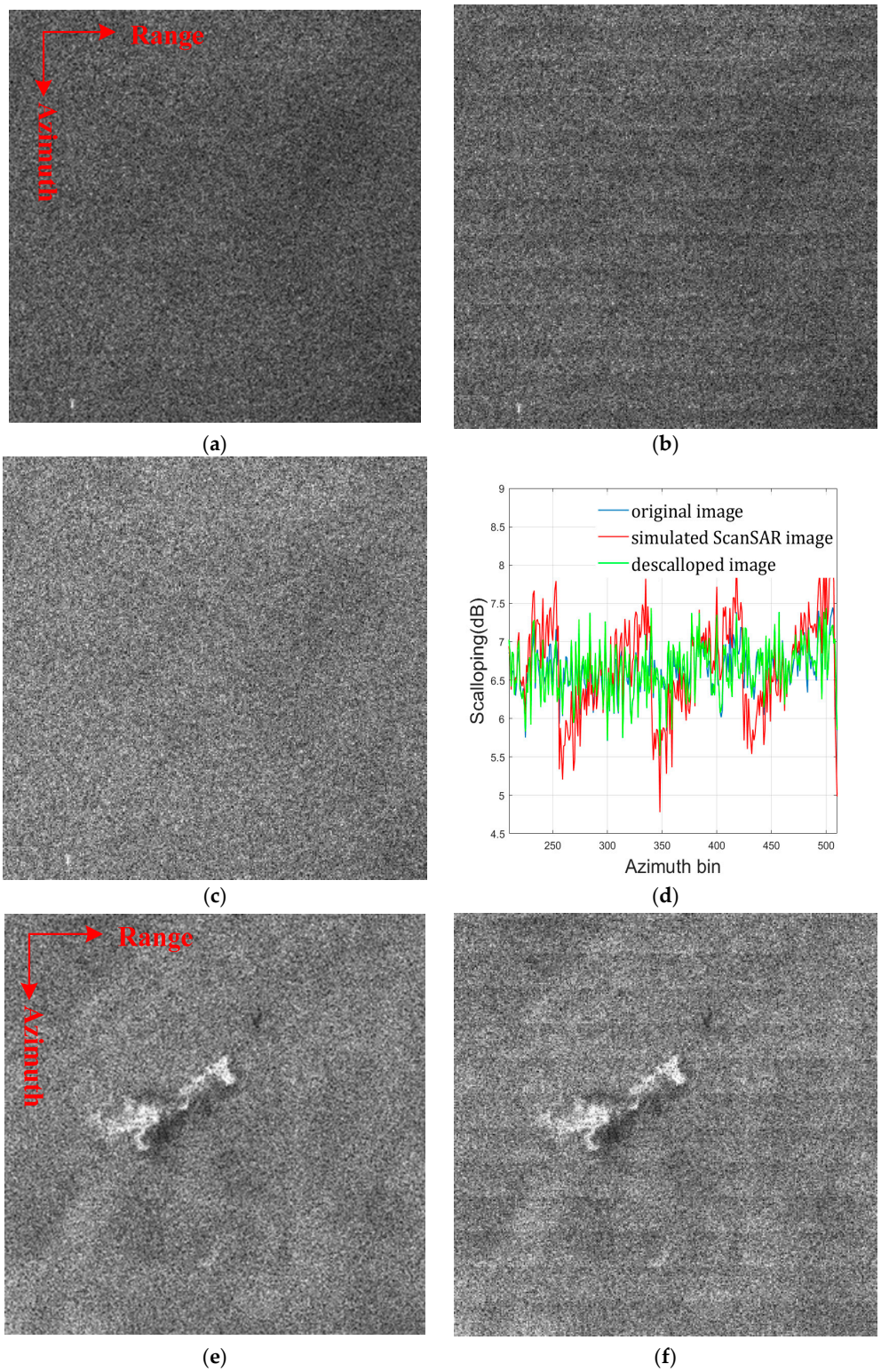
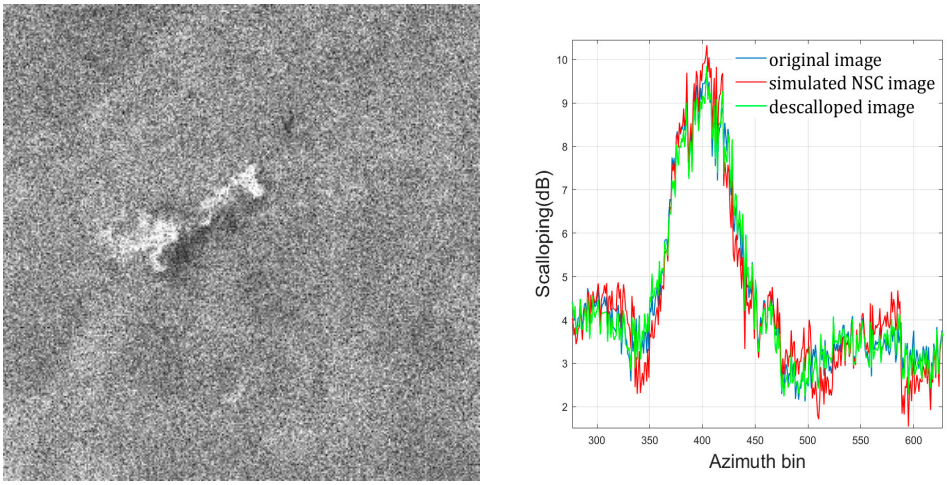


Figure 12. *Cont.*



(**g**) (**h**)

Figure 12. Results of simulated ScanSAR image: (**a**) stationary sea surface in the standard strip (SS) image; (**b**) stationary sea surface in the simulated ScanSAR image; (**c**) stationary sea surface in the descalloped ScanSAR image; (**d**) scalloping comparation of (**a–c**); (**e**) non-stationary sea surface in the SS image; (**f**) non-stationary sea surface in the simulated ScanSAR image; (**g**) non-stationary sea surface in the descalloped ScanSAR image; (**h**) scalloping comparation of (**e–g**).

Figure 12a–c shows the descalloping effect of the stationary sea surface. In the stationary sea surface, the influence of the scalloping is more prominent due to the small fluctuation of the sea surface. After descalloping, the azimuth intensity profile (AIP) calculated according to Equation (18) is shown in Figure 12d. The AIP reflects the undulation of intensity along the azimuth and represents the strength of the scalloping. The blue curve in Figure 12d represents the AIP of the original SS image, the red is the AIP of the simulated NSC image, and the green is AIP of the simulated NSC image after descalloping. From Figure 12d, we can see that the blue and green curves are basically coincident, and the undulation of the red curve is significantly higher than the other two colors, which shows that the descalloping method proposed in this paper can suppress the scalloping well in the simulated NSC image. The residual scalloping is reduced from 1.6 to 0.4 dB.

The scalloping in Figure 12f has a relatively small visual impact on the image due to the large fluctuation of the non-stationary sea surface. Comparing Figure 12g with Figure 12f, the scalloping is also significantly suppressed. At the same time, the descalloped image preserves the texture of the sea surface, which is consistent with the original SS image in Figure 12e. According to the AIP of the images in Figure 12h, after scalloping suppression, the residual scalloping is also less than 0.4 dB.

4.1.3. Statistical Characteristics Analysis

Then, the histograms of the stationary sea surface and non-stationary sea surface before and after descalloping were analyzed to determine whether the sea surface statistical model changed.

The size of the above-selected areas is 1024×1024, which is much larger than the size of a single burst image (42 pixels in the simulated NSC image). It can be seen from Figure 13 that the statistical characteristics of the image changed slightly due to the modulation by scalloping. After descalloping, the statistical properties of the image are restored to the true value, eliminating the modulation effect of scalloping.

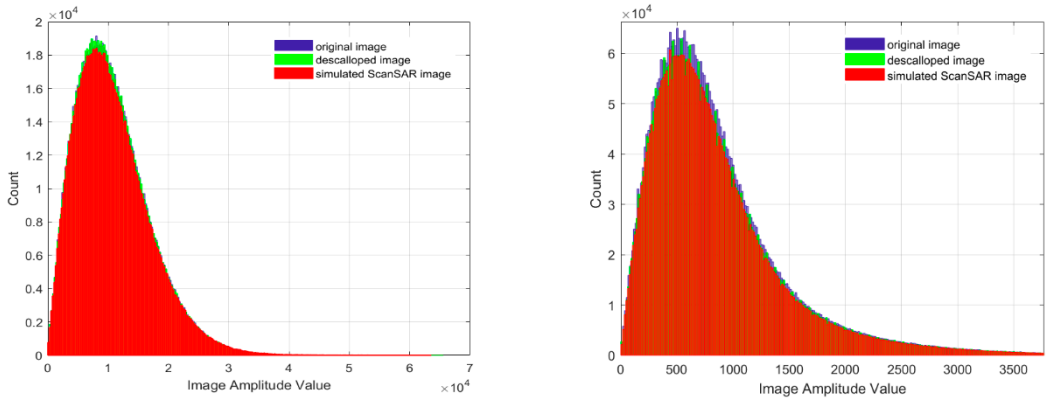


Figure 13. Histogram before and after descalloping: (**a**) uniform sea surface; (**b**) non-uniform sea surface.

4.1.4. Ship Target Analysis

Ship detection and RCS analysis are also important applications of SAR images. In this section, we will analyze the intensity change of the selected ship and the clutter variation surrounding it.

Figure 14 presents the ship slice in the original SS image, the simulated ScanSAR image, and the descalloped ScanSAR image.

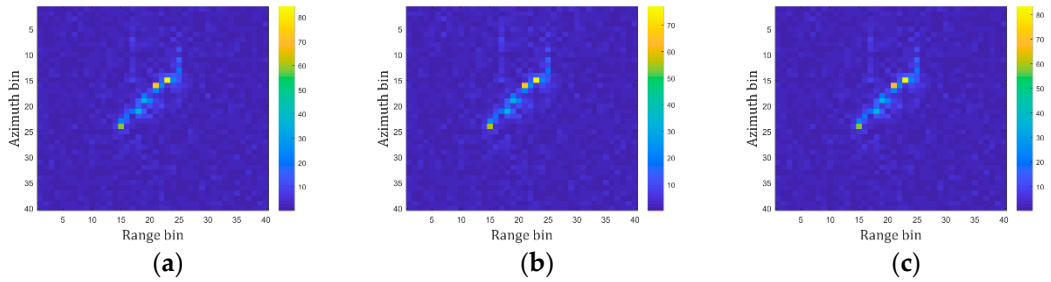


Figure 14. Descalloping effect on the ship: (**a**) ship in the SS image; (**b**) ship in the simulated ScanSAR image; (**c**) ship in the descllloping image.

Table 2 shows the peak intensity and clutter strength of the ship in three images.

Table 2. Effects of descalloping on ships.

	SS Image	Simulated ScanSAR Image	Descalloping Image
Peak intensity (dB)	38.53	37.73	38.43
Clutter strength (dB)	9.32	9.19	9.27

The outline of the ship remains consistent in the image before and after scalloping suppression, and the peak intensity of the target increases 0.8 dB after scalloping suppression. The intensity error is only 0.1 dB from the actual target in Figure 14a. The variation of clutter near the ship is less than 0.15 dB before and after descalloping.

The area selected for calculating the clutter strength is 40×40 pixels around the ship, which is exactly close to the azimuth size of a burst in the azimuth direction, namely, a period of scalloping. In one period, the overall intensity is approximately constant due to the near-linear modulation of the image by scalloping. However, the ship is at the lower end of the modulation curve, and the peak intensity becomes smaller when modulated. After scalloping suppression, the modulation of scalloping texture on the target intensity is eliminated. Compared with the simulated ScanSAR image,

the target intensity is closer to the real value in the descalloped image. Therefore, more accurate scattering characteristics of the target can be obtained from the descalloped image.

4.2. Real Data of GF-3

4.2.1. Experimental Results of Ocean Scenes

In this section, we will use a typhoon image to analyze and verify the effect of scalloping suppression in ocean scenes. The image shown in Figure 15 is the 9th typhoon named "Nesat". The image is acquired by GF-3 on July 29, 2017, using NSC mode when the typhoon passes through eastern Taiwan, China. Frame 1 is the location of the typhoon eye and Frame 2 is the coastline. Figures 16 and 17 show the comparison between original images and descalloping results.

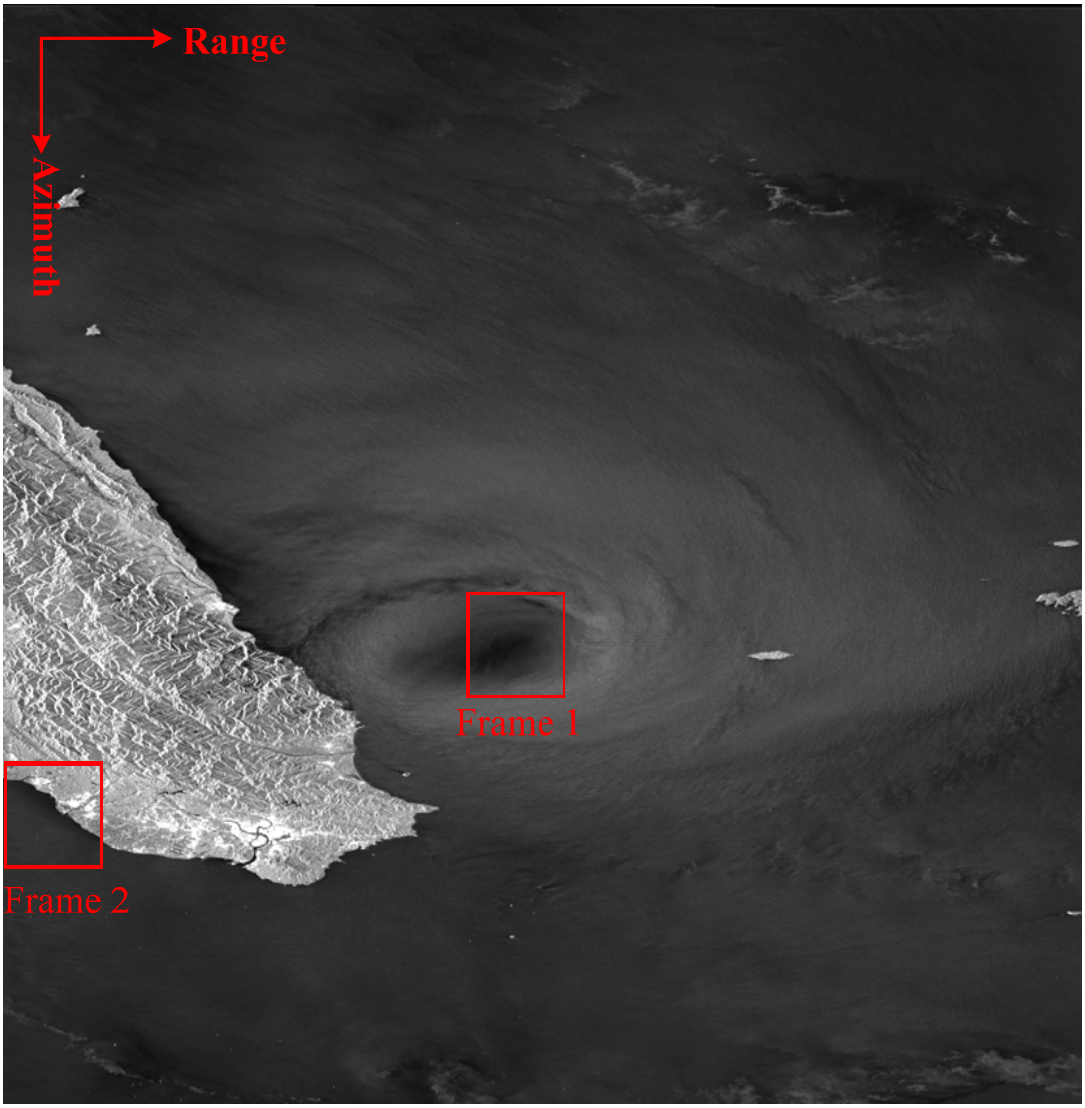
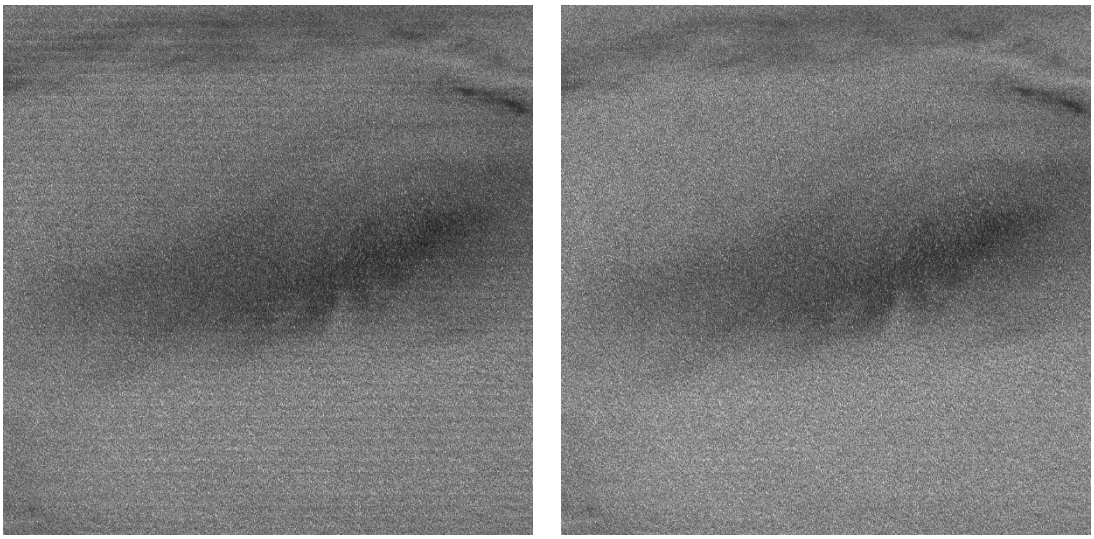
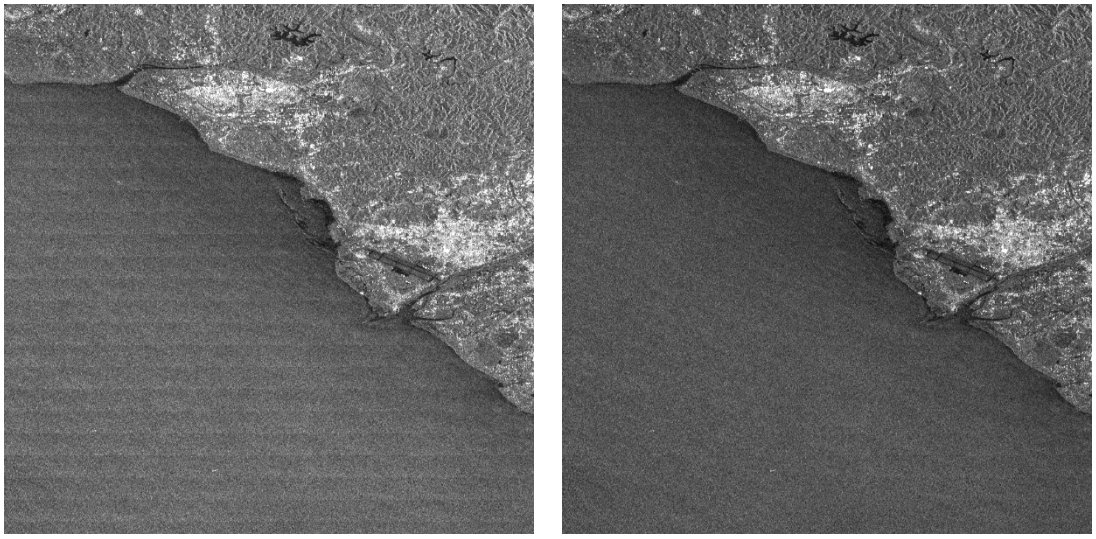


Figure 15. Descalloping result of ocean image: Scene ID: 3935909; Imaging Mode: NSC; Polar Mode: HH; Date: 2017-07-29; Area: Taiwan, China.



(**a**) (**b**)

Figure 16. Comparation before and after descalloping of the typhoon eye: (**a**) Frame 1 of Figure 15 before descalloping; (**b**) image after descalloping of (**a**).



(**a**) (**b**)

Figure 17. Comparation before and after descalloping of interface between land and sea: (**a**) Frame 2 of Figure 15 before descalloping; (**b**) image after descalloping of (**a**).

It can be seen that after scalloping suppression in the above two areas, the texture of scalloping disappears invisibly. In Figures 16 and 17, the contrast before and after scalloping suppression on the sea surface is obvious, but the fluctuation of the scene on the land is much larger than that of scalloping texture, so the visual improvement of the land is not obvious. Quantitative analysis of the descalloping effect is shown in Figure 18. The residual scalloping is suppressed from 1.0 to 0.4–0.5 dB.

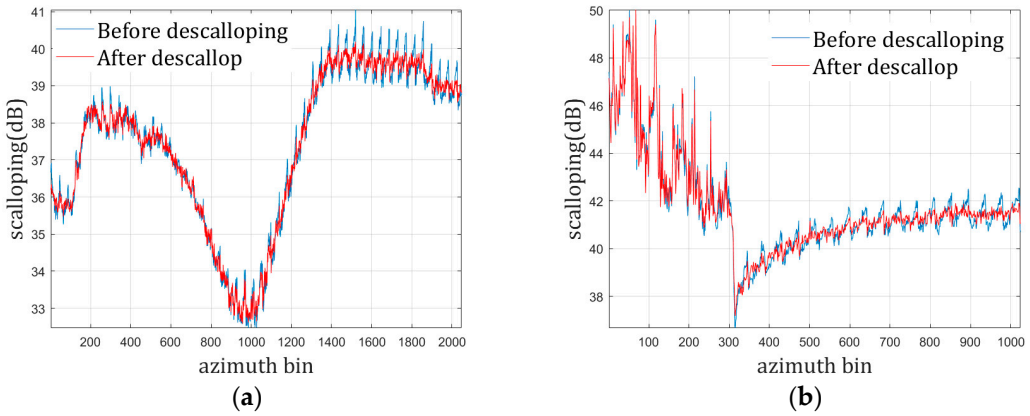


Figure 18. Scalloping profiles before and after descalloping: (**a**) scalloping profiles of Figure 16a,b; (**b**) scalloping profiles of Figure 17a,b.

4.2.2. Experimental Results of the Non-Uniform Scene

The image of Bohai bay acquired by GF-3 was used to analyze the effectiveness of the algorithm in non-uniform scenes. The original image is shown in Figure 8 and the image after descalloping is shown in Figure 19. As described in Section 3.3, the image includes a large number of vessels in Bohai bay, a large number of port infrastructures along the coast, marine aquaculture facilities, etc.

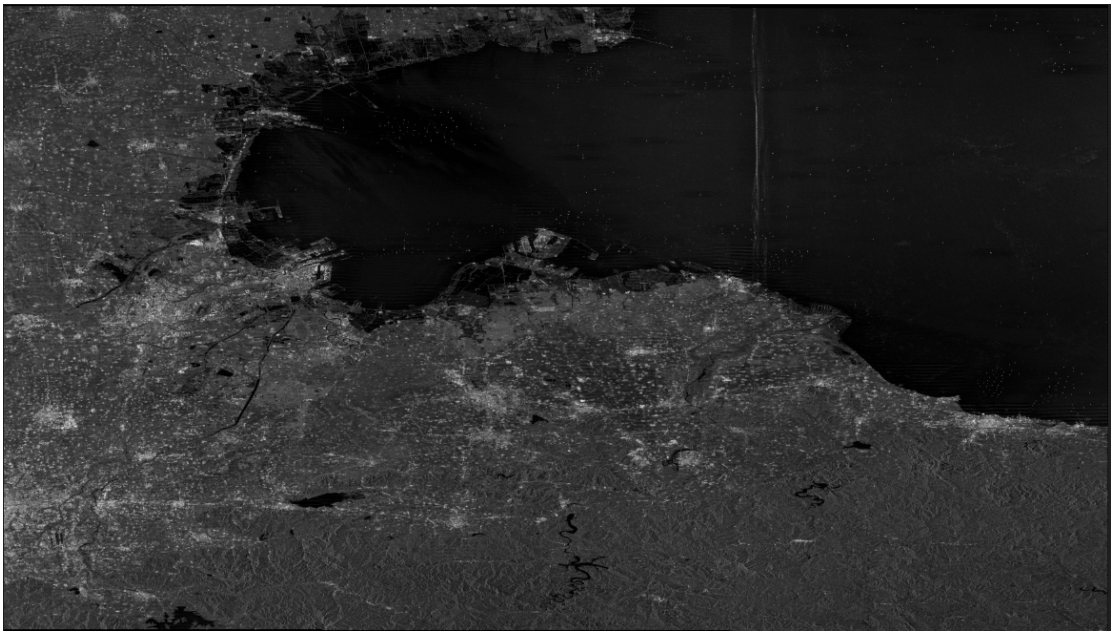


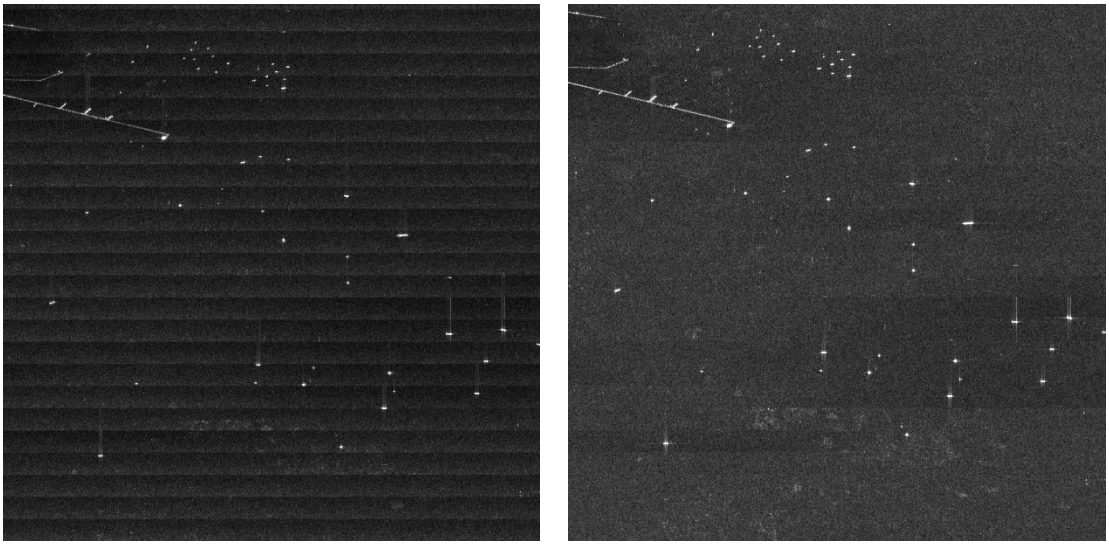
Figure 19. ScanSAR image of GF-3 in Bohai bay area.

We analyzed the two areas marked by the red frame in Figure 8 to verify the effect of the proposed descalloping method. According to the analysis in Section 3.3, Frame 1 is considered to be a non-uniform scene, while Frame 2 is considered to be a uniform scene. For Frame 2, the features of scalloping can be extracted from itself, while for Frame 1, the features of scalloping need to be obtained from Frame 2 and other uniform scenes. The scalloping suppression results of Frame 1 and 2 are shown in Figures 20 and 21, respectively.



(**a**) (**b**)

Figure 20. Descalloping effect of Bohai bay: (**a**) before descalloping; (**b**) after descalloping.



(**a**) (**b**)

Figure 21. Descalloping effect of ships: (**a**) before descalloping; (**b**) after descalloping.

The scene in Figure 20a changes gradually from land to port to ocean. As the intensity fluctuation near the land and port is greater than that of scalloping, compared with Figure 20b, the left hand of Figure 20a changes little before and after descalloping. However, the scalloping in the sea area on the right hand of Figure 20a is effectively suppressed, and the sea area changed significantly in the images before and after the scalloping suppression.

In Figure 21, the contrast before and after scalloping suppression is obvious. The texture of scalloping in the image is eliminated well. The brightness in the area marked by the white frame in the image is lower than the brightness of the nearby sea surface. This is due to the block adaptive quantization (BAQ) for echo data, rather than caused by residual scalloping.

5. Discussion

The method proposed in this paper was confirmed by processing the simulation and real data, and the real data of GF-3 in NSC mode were used to illustrate the descalloping effect in different scenarios. Experimental results show that residual scalloping can be reduced to 0.5dB in different scenarios.

For wind and wave retrieval, Romaier et al. performed scalloping suppression on the image products of RADARSAT-1 and TERRASAR. The image domain descalloping algorithm requires accurate identification of scalloping. Romaier's method needs to search and detect the harmonics in the spectrum. However, as shown in Figure 9, the characteristic harmonics of scalloping in the non-uniform scene are masked by the spectrum of the scene, and it is necessary to adopt sea–land segmentation and ship mask in Romaier's method. We focused on imaging processing and radiometric correction [28,29], therefore, we suppressed scalloping in combination with imaging parameters during the imaging process. As shown in Figures 7 and 9d, we can accurately calculate the positions of harmonics by the imaging parameters to avoid searching and detecting in the spectrum. Therefore, our method does not need to carry out sea–land segmentation and ship mask.

In addition, scalloping texture is affected by factors such as noise and image stitching, which is not considered enough in former research. We used the subswath image before splicing to avoid the influence of the azimuth misalignment of the scalloping in the adjacent subswath seams. The modulated noise increases the scalloping under low SNR conditions. The modulated noise is also periodic, and the spectral position of the harmonics is the same as the scalloping caused by doppler centroid error. The two different types of scalloping can be filtered together. However, due to the different SNR, the scalloping caused by noise in different regions is also different. When the sea surface is used to obtain the scalloping texture to suppress the non-uniform scenes such as land and coastline area, the scalloping characteristics of the two are not consistent, which will lead to deterioration of the suppression effect. Therefore, although the scalloping of the weak scene itself can be filtered, for the whole image, it is still necessary to correct the scalloping introduced by the noise first, and then suppress and get the texture of the scalloping introduced by Doppler centroid error.

6. Conclusions

To eliminate scalloping caused by the special working mechanism of ScanSAR mode, this paper proposed an improved descalloping method for ScanSAR image combined with imaging parameters. We deduced the periodic model of scalloping in the image domain, and calculated the precise positions of harmonics caused by scalloping in the frequency spectrum according to the imaging parameters. The proposed method can provide accurate locations for frequency filtering without searching and detecting. For the low SNR scene, we modified the AAP according to SNR to adopted radiometric correction, the scalloping caused by noise was effectively suppressed, and the image intensity was closer to the backscattering coefficient of the scene. We distinguished uniform scene from non-uniform scene by the characteristics of harmonics, so as to avoid the dependence on the external chart data. Scalloping texture was derived from the uniform scene and used to suppress the scalloping of the non-uniform scene. By combining imaging parameters, SNR, subswath splicing information, and other parameters, the proposed method can accurately identify the harmonics of scalloping, and has a better scalloping suppression effect for scenes with low SNR and at the subswath seams. We used different scenes of GF-3 ScanSAR images to verify the effectiveness of the proposed method. Experimental results show that the residual scalloping reduced from 1.0 to 0.3–0.5dB through the verification of GF-3 ScanSAR images, and the image quality was effectively improved.

Author Contributions: Conceptualization, L.Z.; methodology, L.Z. and X.Q.; investigation, L.Z.; resources, L.Z. and B.H.; supervision, Y.H.; writing—original draft preparation, L.Z.; writing—review and editing, X.Q., B.H., and Y.H. All authors have read and agreed to the published version of the manuscript.

Funding: This work is supported by the National Natural Science Foundation of China (NSFC), grant numbers 61991421, 61991420 and 41976169.

Acknowledgments: The authors wish to acknowledge the support of the Gaofen-3 mission, especially the National Satellite Ocean Application Service and the China Centre for Resources Satellite Data and Application.

Conflicts of Interest: The authors declare no conflict of interest.

References

1. Raney, R.; Luscombe, A.; Langham, E.; Ahmed, S. Radarsat [sar imaging]. *Proc. IEEE* **1991**, *79*, 839–849. [CrossRef]
2. Mittermayer, J.; Moreira, A.; Davidson, G.; Bamler, R.; Desnos, Y. High precision processing of SIR-C ScanSAR data. In Proceedings of the IEEE International Geoscience and Remote Sensing Symposium (IGARSS 1996), Lincoln, NE, USA, 31–31 May 1996.
3. Zink, M.; Buck, C.; Suchail, J.-L.; Torres, R.; Bellini, A.; Closa, J.; Desnos, Y.-L.; Rosich, B. The radar imaging instrument and its applications: ASAR. *ESA Bull.* **2001**, *106*, 46–55.
4. Steinbrecher, U.; Kraus, T.; Alfonzo, G.; Grigorov, C.; Benjamin, B. TerraSAR-X: Design of the new operational WideScanSAR mode. In Proceedings of the European Conference on Synthetic Aperture Radar (EUSAR 2014), Berlin, Germany, 3–5 June 2014.
5. Natsuaki, R.; Motohka, T.; Shimada, M.; Suzuki, S. Burst misalignment evaluation for ALOS-2 PALSAR-2 scansar-scansar interferometry. *Remote Sens.* **2017**, *9*, 216. [CrossRef]
6. Morena, L.; James, K.; Beck, J. An introduction to the RADARSAT-2 mission. *Can. J. Remote Sens.* **2004**, *30*, 221–234. [CrossRef]
7. Flett, D.; Crevier, Y.; Girard, R. The RADARSAT Constellation Mission: Meeting the government of Canada's needs and requirements. In Proceedings of the IEEE International Geoscience and Remote Sensing Symposium (IGARSS 2009), Cape Town, South Africa, 12–17 July 2009.
8. Thompson, A.A. Innovative Capabilities of the RADARSAT Constellation Mission. In Proceedings of the European Conference on Synthetic Aperture Radar (EUSAR 2010), Aachen, Germany, 7–10 June 2010.
9. Davidson, G.; Mantle, V.; Bernhard, R.; Williams, D.; Geudtner, D. Implementation of Tops Mode on RadarSAT-2 In Support of The Sentinel-1 Mission. In Proceedings of the ESA Living Planet Symposium, Edinburgh, UK, 9–13 September 2013.
10. Zhang, L.; Liu, H.; Gu, X.; Guo, H.; Chen, J.; Liu, G. Sea Ice Classification Using TerraSAR-X ScanSAR Data With Removal of Scalloping and Interscan Banding. *IEEE J. Sel. Top. Appl. Earth Obs. Remote Sens.* **2019**, *12*, 589–598. [CrossRef]
11. Vigneron, C. Radiometric Image Quality Improvement of ScanSAR Data. Master's Thesis, The University of British Columbia, Vancouver, BC, Canada, 1996.
12. Bamler, R. Optimum look weighting for burst-mode and ScanSAR processing. *IEEE Trans. Geosci. Remote Sens.* **1995**, *33*, 722–725. [CrossRef]
13. Anfinsen, S.N.; Doulgeris, A.P.; Eltoft, T. Estimation of the equivalent number of looks in polarimetric synthetic aperture radar imagery. *IEEE Trans. Geosci. Remote Sens.* **2009**, *47*, 3795–3809. [CrossRef]
14. Touzi, R. A review of speckle filtering in the context of estimation theory. *IEEE Trans. Geosci. Remote Sens.* **2002**, *40*, 2392–2404. [CrossRef]
15. Shimada, M. A New Method for Correcting ScanSAR Scalloping Using Forests and Inner-Scan Banding Employing Dynamic Filtering. *IEEE Trans. Geosci. Remote Sens.* **2009**, *47*, 3933–3942. [CrossRef]
16. Bamler, R. Doppler Frequency Estimation and the Cramer-Rao Bound. *IEEE Trans. Geosci. Remote Sens.* **1996**, *29*, 385–390. [CrossRef]
17. Jin, M. Optimal Doppler Centroid Estimation for SAR Data from Quasi-homogeneous source. *IEEE Trans. Geosci. Remote Sens.* **1986**, *23*, 1022–1025. [CrossRef]
18. Dragosevic, M.V.; Plache, B. Doppler tracker for a spaceborne ScanSAR system. *IEEE Trans. Aerosp. Electron. Syst.* **2000**, *36*, 907–924. [CrossRef]
19. Cafforio, C.; Guccione, P.; Guarnieri, A.M. Doppler centroid estimation for scansar data. *IEEE Trans. Geosci. Remote Sens.* **2004**, *42*, 14–23. [CrossRef]
20. Jin, M. Optimal Range and Doppler Centroid Estimation for a ScanSAR System. *IEEE Trans. Geosci. Remote Sens.* **1996**, *34*, 479–488. [CrossRef]
21. Schiavulli, D.; Sorrentino, A.; Migliaccio, M. An Innovative Technique for Postprocessing Descalloping. *IEEE Geosci. Remote Sens. Lett.* **2013**, *10*, 424–427. [CrossRef]
22. Iqbal, M.; Chen, J. Removal of scalloping in ScanSAR images using Kalman filter. In Proceedings of the IEEE International Geoscience and Remote Sensing Symposium (IGARSS 2012), Munich, Germany, 22–27 July 2012.
23. Romeiser, R. A Dscalloping Postprocessor for ScanSAR Images of Ocean Scenes. *IEEE Trans. Geosci. Remote Sens.* **2013**, *51*, 3259–3272. [CrossRef]

24. Sun, J.; Yu, W.; Deng, Y. The SAR Payload Design and Performance for the GF-3 Mission. *Sensors* **2017**, *17*, 2419. [CrossRef]
25. Shao, W.; Ding, Y.; Li, J.; Gou, S.; Nunziata, F.; Yuan, X.; Zhao, L. Wave Retrieval Under Typhoon Conditions Using a Machine Learning Method Applied to Gaofen-3 SAR Imagery. *Can. J. Remote Sens.* **2019**, *45*, 1–10. [CrossRef]
26. Zhang, T.; Li, X.; Feng, Q.; Ren, Y.; Shi, Y. Retrieval of Sea Surface Wind Speeds from Gaofen-3 Full Polarimetric Data. *Remote Sens.* **2019**, *11*, 813. [CrossRef]
27. Liu, Z.; Liu, B.; Guo, W.; Zhang, Z.; Zhang, B.; Zhou, Y.; Ma, G.; Yu, W. Ship Detection in GF-3 NSC Mode SAR Images. *J. Radars* **2017**, *6*, 473–482.
28. Han, B.; Ding, C.; Zhong, L.; Liu, J.; Qiu, X.; Hu, Y.; Lei, B. The GF-3 SAR Data Processor. *Sensors* **2018**, *18*, 835. [CrossRef] [PubMed]
29. Han, B.; Zhong, L.; Liu, J.; Qiu, X.; Hu, Y.; Lei, B. SAR Data Processing for GF3. In Proceedings of the 12th European Conference on Synthetic Aperture Radar (EUSAR 2018), Aachen, Germany, 5–7 June 2018.
30. Moreira, A.; Mittermayer, J.; Scheiber, R. Extended chirp scaling algorithm for air and spaceborne SAR data processing in stripmap and ScanSAR imaging modes. *IEEE Trans. Geosci. Remote Sens.* **1996**, *34*, 1123–1136. [CrossRef]
31. Zhang, Q. System Design and Key Technologies of the GF-3 Satellite. *Acta Geod. Cartogr. Sin.* **2017**, *46*, 269–277.
32. Zhou, J.; Wei, Y.; Cao, Y.; Sun, K.; Ma, Y.; Yuan, J. AOCS Design and On-orbit Verification of GF-3 Satellite. *Spacecr. Eng.* **2017**, *26*, 93–98.
33. Romeiser, R.; Alpers, W.; Wismann, V. An improved composite surface model for the radar backscattering cross section of the ocean surface: 1. Theory of the model and optimization/validation by scatterometer data. *J. Geophys. Res. Ocean.* **1997**, *102*, 25237–25250. [CrossRef]
34. Freeman, A.; Curlander, C. Radiometric Correction and Calibration of SAR Images. *Photogramm. Eng. Remote Sens.* **1989**, *55*, 1295–1301.
35. Hawkins, R.; Vachon, P. Modelling SAR Scalloping in Burst Mode Products from RadarSAT-1 and ENVISAT. In Proceedings of the CEOS Working Group on Calibration/Validation SAR Workshop, London, UK, 24–26 September 2002.



© 2020 by the authors. Licensee MDPI, Basel, Switzerland. This article is an open access article distributed under the terms and conditions of the Creative Commons Attribution (CC BY) license (http://creativecommons.org/licenses/by/4.0/).